Available online at www.sciencedirect.com
ScienceDirect
International Journal of Heat and Fluid Flow 27 (2006) 924–936
International Journal of HEAT AND FLUID FLOW
www.elsevier.com/locate/ijhff

Experimental characterization and modelling of inflow conditions for a gas turbine swirl combustor

R. Palm, S. Grundmann, M. Weismüller, S. Šarić, S. Jakirlić *, C. Tropea

Chair of Fluid Mechanics and Aerodynamics, Darmstadt University of Technology Petersenstr. 30, 64287 Darmstadt, Germany

Received 5 October 2005; received in revised form 23 January 2006; accepted 4 March 2006
Available online 15 June 2006

Abstract

One of the most important processes in a gas turbine combustor, influencing to a large extent the efficiency of the entire combustion process, is the mixing between a swirling annular jet (primary air) and the non-swirling inner jet (fuel). To study this fundamental flow geometry an experimental facility has been built which allows independent flow rate adjustment of the central (mean stream) and co-axial jet flow $\dot{m}_c/\dot{m}_m$ and furthermore, good optical access for laser-based flow measurement techniques. Other important flow parameters include the Reynolds number, the swirl intensity (S) and the combustor confinement, expressed in terms of an area expansion ratio (ER). The work presented focuses on features of the swirling flow in the concentric annuli part of the inlet system. The laser Doppler technique has been used to measure the velocity profile and the gradient of the velocity in the annular cross section. The circumferential velocity profile follows the so-called free-vortex flow type, being characterized by an increase in the mean angular momentum with radius of curvature. The outcome of the experiment is that the axial velocity profile becomes increasingly asymmetric with increased swirl intensity. The velocity increases from the inside to the outside of the annular flow (with a decreasing gradient at the inner wall) corresponding to an intensified radial movement towards the outer wall due to imposed swirl. The numerical investigations, especially those accounting for the complete swirl generation system and using a second-moment closure reproduced all important mean flow and turbulent features in good agreement with available experimental data. In addition, both the modelling and the Large Eddy Simulations of equilibrium, fully-developed swirling flow in the annular inlet pipe performed separately in course of the inflow data generation, revealed some interesting departures with respect to the sign of the axial velocity gradient.

Keywords: Swirl combustor; Swirling annular inflow; Laser Doppler measurements; Large Eddy Simulation; Turbulence modelling; Second-moment closure

1. Introduction

A general interest to reduce fossil fuel consumption and recent regulatory measures to limit combustion emissions create demands to increase the efficiency and performance of combustion chambers. For a clean and controlled combustion a fine and homogeneous spray is necessary. This can be achieved by using a swirling free shear layer, see Fig. 1. The free swirl-induced recirculation area leads to a stable flame and creates a homogeneous spray inside the flue. The flow is characterised by a high level of turbulence and strong streamline curvature. This complex flow geometry is also a good example of where experimental and numerical investigations can be complementary. The experimental results can be used as verification data for turbulence models and numerical simulations, which are more economical for parametric investigations.

The common practice when computing the combustor flows numerically is that the inlet cross-section of the solution domain typically coincides with the first available measurement location, usually being situated in the interior of the combustor, e.g., Lai (1996). In that case the inlet plane crosses both the corner bubble and the large recirculation zone in the core flow. The measurement data commonly

* Corresponding author. Tel.: +49 6151 16 3554; fax: +49 6151 16 4754.
E-mail address: s.jakirlic@sla.tu-darmstadt.de (S. Jakirlić).

0142-727X/$ - see front matter © 2006 Elsevier Inc. All rights reserved.
doi:10.1016/j.ijheatfluidflow.2006.03.016

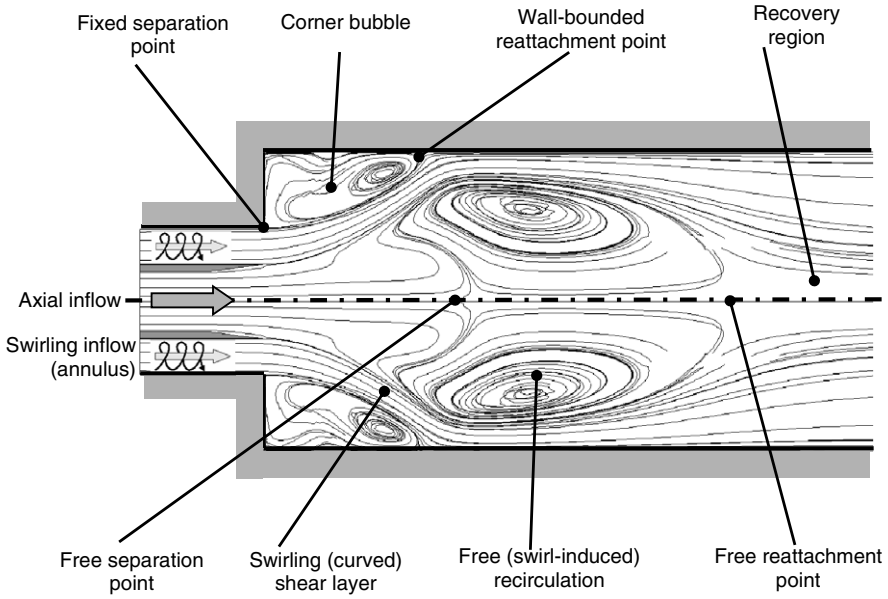

Fig. 1. Schematic of air flow in an idealized combustion chamber.

exhibit a certain scatter in this flow region and are often incomplete. Such a computational practice is especially unsuitable when specifying the dissipation rate of the kinetic energy of turbulence and the scalar profiles along the inlet boundary. Furthermore, the flow configuration is reduced to a pipe geometry, unlike the geometry of the sudden expansion being typical for a combustor. Hence, the influence of the flow expansion – adverse pressure gradient – cannot be accounted for. Another possibility encountered in the literature is to extrapolate backwards the experimental results from the first available measurement location situated in the interior of the combustor to the combustor inlet, which usually coincides with the inlet cross-section of the solution domain, by preserving the mass flow rate and angular momentum, e.g., Wennerberg and Obi (1993). This method is however wrought with numerous uncertainties. The most direct way is to compute the flow in the swirl generator. However, it is numerically too demanding, especially if high resolution computational schemes (e.g., LES) are to be applied. The generation of the inflow data by performing a separate calculation is regarded as a better choice. Pierce and Moin (1998) proposed a simple, but efficient method for generating the swirling inflow data. The method is based on the computation of the fully developed, annular, swirling flow, imposing a uniform profile of the fictitious azimuthal pressure gradient (azimuthal body force). The method proved its credibility in the Large Eddy Simulation of the Roback and Johnson (1983) case. However, the uncertainty in the data structure obtained computationally is still present. In general it is much more desirable to have experimental reference data for comparison.

Numerous experimental investigations, serving for years as benchmarks for computational methods and turbulence model validation[1] are known in the open literature, e.g., Roback and Johnson (1983), So et al. (1984), Nejad et al. (1989), Dellenback et al. (1988), etc. However, none of them offers information about the flow within the inlet section. These circumstances motivated a systematic experimental investigation of the influence of the swirl intensity and mass flow rate ratio of the annular stream (representing primary air) to the central jet (representing fuel) on the flow, mixing (passive scalar transport) and associated turbulence with emphasis on the near-field region of the flue characterized by the most intensive mixing. The present, tubo-annular combustor geometry (Fig. 2) represents an idealization of a can-type combustor investigated experimentally by Heitor and Whitelaw (1986). The present combustor was built substantially longer ($L_f = 1200$ mm, Table 2) in order to minimize the influence of the outflow on the near field. Such a combustor type belongs to the older generation of the gas turbines, being no longer in use. A more common geometry for gas turbines is nowadays the ring-shaped combustor, that is a single-annular combustor (e.g., Hassa et al., 1998). However, in both combustor types the inlet system – swirl generator and concentric annuli pipe – is almost identical (important differences are present only with respect to the structure of the central stream, which is usually counter swirling in a single-annular combustor). Because of that, special attention was devoted here to the characteristics of the swirling annular inflow, being very similar in both configurations. The experimental investigations have been performed within a range of mean flow Reynolds numbers, mass flow rate ratios, swirl intensities and expansion ratios, Table 1

[1] See e.g., Hogg and Leschziner (1989), Wennerberg and Obi (1993), Lai (1996) and Jakirlic et al. (2002).

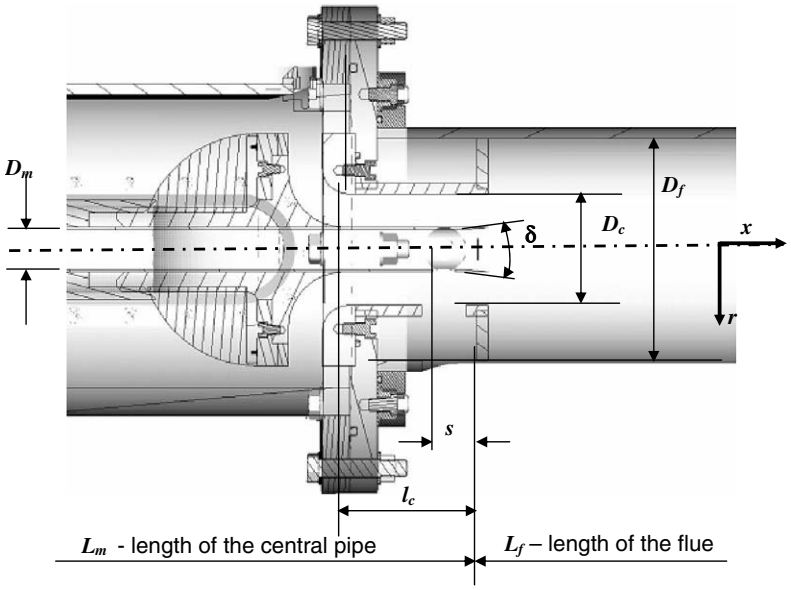

Fig. 2. Combustion chamber model.

Table 1
Operating parameters of the combustion chamber

Parameter	Range
Reynolds number (Main flow)	$23.500 \leqslant Re_m \leqslant 102.000$
Mass flow rate (Main flow)	$0.011\ \text{kg/s} \leqslant m \leqslant 0.048\ \text{kg/s}$
Reynolds number (Annular flow)	$50.500 \leqslant Re_c \leqslant 125.500$
Mass flow rate (Annular flow)	$0.1\ \text{kg/s} \leqslant \dot{m} \leqslant 0.25\ \text{kg/s}$
Swirl intensities	$0 \leqslant S \leqslant 1.2$
Expansion ratio	1.5 and 2.0

Table 2
Dimensions of the facility

Identification of the tube	Inner (D_i)/outer(D_o) Diameter
Main flow	$D_{m,i} = 36\ \text{mm}/D_{m,o} = 40\ \text{mm}$
Length of the central pipe	$L_m = 720\ \text{mm}$
Coaxial flow	$D_{c,i} = 40\ \text{mm}/D_{c,o} = 100\ \text{mm}$
Length of the annular pipe	$L_c = 120\ \text{mm}$
Flue ($ER = 2$)	$D_f = 200\ \text{mm}$
Flue ($ER = 11.5$)	$D_f = 150\ \text{mm}$
Length of the flue	$L_f = 1200\ \text{mm}$
Diffuser angle	$\delta = 7.5°$

(only the results obtained for the expansion ratio $ER = 2$ will be shown here). The present work provides the profiles of both the axial and circumferential velocity and all six non-zero Reynolds stresses for a range of swirl numbers $S = 0.0$–1.2 and two different mass flow rates $\dot{m}_c = 0.1$ and 0.25 kg/s, corresponding to the Re_c numbers (based on the hydraulic diameter $D_h = D_{c,o} - D_{c,i}$) of 50,500 and 125,500 respectively, in the cross-section of the concentric annulus.

Numerous experimental studies of swirling flow in an annulus formed between two concentric stationary[2] cylinders have also been published. Clayton and Morsi (1984, 1985) investigated experimentally (using hot-wire anemometry and flow visualization) the mean flow (velocity and pressure) and turbulence evolution focussing on the swirl decay in a fairly long concentric annulus (>1 m) for different Reynolds numbers (up to $Re_c \approx$ 30,000) and swirl intensities (expressed in terms of the guide vane setting angle: $\Psi = 0$–$60°$). A similar study at much higher Reynolds numbers in a 1.8m long concentric annulus was conducted by Yowakim and Kind (1988). Clayton and Morsi gave also an overview about related investigations. All of these results indicate an increasingly asymmetric shape of the axial velocity profile with increased swirl intensity, whose maximum was shifted towards the outer wall. However, a substantial portion of the cross-section in the developing part of the annulus corresponds to a core (potential-like) flow with a flat velocity profile. Accordingly, the turbulent stress profiles exhibited a shape typical for a channel/pipe flow with minima in the flow core and maxima in the wall region. While some important similarities between these investigations and the present study exist, especially with respect to the mean flow asymmetry and associated difference between the shear stresses at the inner and outer wall, it should be stressed that the flow in the present, fairly short (only 120 mm) cylindrical annulus, is much more complex. The annulus represents a part of the inlet section of an actual combustor. It is situated immediately behind the swirl generator. The weakly compressible flow in the swirl generator exhibits both the swirl-induced recirculation regions and the flow reversal originating from the vortex shedding from the movable blocks, the latter serving for the swirl intensity regulation (see Section 4.1). It influences the turbulent structure in the annulus to a large extent.

Complementary to the experimental investigations, a computational study covering both configurations the entire swirl generation system (including swirl generator

[2] Fully developed flow between a rotating inner cylinder and a stationary outer cylinder was experimentally studied by Nouri and Whitelaw (1994) and investigated computationally by means of Large Eddy Simulation by Chung and Sung (2005).

and annular pipe) and the flow in the concentric annulus, assuming a fully developed flow, was conducted. Hereby, both Reynolds–Averaged Navier–Stokes (RANS) approach and Large-Eddy Simulation method were applied.

2. Experimental facility

For the investigation of flow and mixing, a single tubo-annular swirl combustor (Fig. 2) has been constructed. The modular assembly allows velocity measurements directly after the swirl generator. This was realised by mounting an extended annular tube after the swirl generator, before the flow enters the flue. Table 1 summarizes the operating parameters of the experimental facility, which have been chosen to represent values typical of a real combustor.

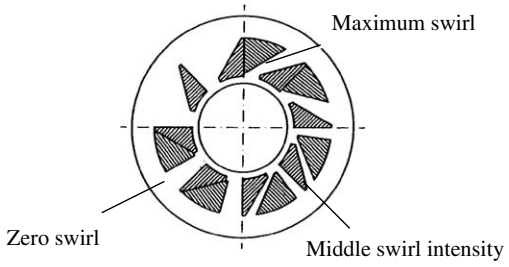

Fig. 3. Principle of the movable block swirl generator.

2.1. Design of the swirl generator

The swirl generator is based on the "movable block" design (Leuckel, 1969, see Fig. 3). By rotating an inner and an outer annular block relative to each other, varying degrees of tangential and radial channels will be created. With a pure radial inlet, a non-swirling flow will be obtained (lower left) and with a pure tangential inlet the maximum swirl is generated (upper right). The swirl generator (Fig. 4) yields a swirl number in the range $0 \leqslant S \leqslant 1.2$. The swirl number S is defined in Eq. (1) and is a bulk quantity describing the swirl intensity. The swirl number is the ratio of the angular momentum flow ($\dot{D}$) to the product of the axial impulse flow ($\dot{I}$) and the radius (R) as a characteristic length.

$$S = \frac{\dot{D}}{R \cdot \dot{I}} = \frac{2\pi \int_{R_i}^{R_o} \rho \bar{u}\bar{w} r^2 \, \mathrm{d}r}{R \cdot 2\pi \int_{R_i}^{R_o} \rho \bar{u}^2 r \, \mathrm{d}r} \tag{1}$$

2.2. Measurement details

A two-velocity component laser Doppler instrument operated in backscatter was used to measure velocity profiles across the annular entrance channel before the flue. Optical access is provided through appropriate windows, Fig. 5. Both a horizontal and a vertical optical access of the laser Doppler probe to the annular flow is available, allowing all three components of velocity (two at a time)

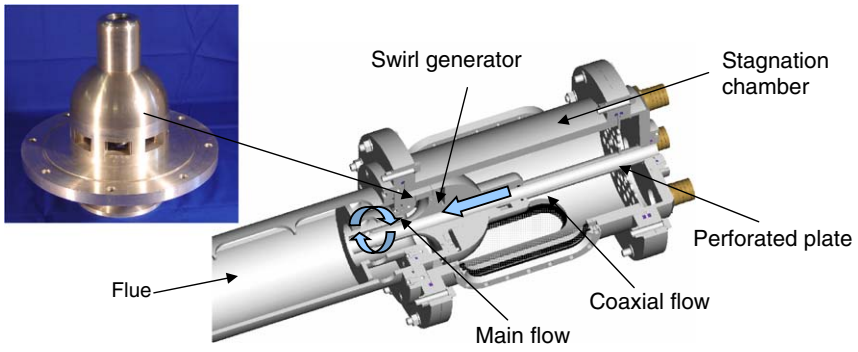

Fig. 4. Assembly of swirl generator (left) and integration inside the entrance chamber (right).

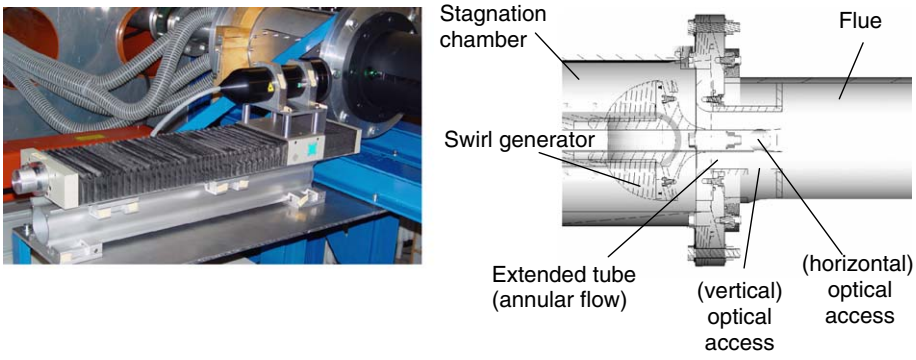

Fig. 5. Optical access for the LDV probe head.

to be measured. The axial velocity is measured once redundantly, useful for checking the reproducibility of the results. All velocity profiles were taken 40 mm upstream of the sudden expansion. The facility was operated at a matrix of the following parameters:

- Swirl generator block position: $\xi = 0°$, $\xi = 15°$ and $\xi = 30°$.
- Mass flow rate of main (central) non-swirled stream, $\dot{m}_m$ (kg/s):0.010 ($Re_m = 23{,}500$); 0.025 ($Re_m = 47{,}000$) and 0.050 ($Re_m = 102{,}000$).
- Mass flow rate of swirling co-flow, $\dot{m}_c$(kg/s): 0.10 ($Re_c = 50{,}500$) and 0.25 ($Re_c = 125{,}500$).

Seeding particles were introduced into the flow upstream of the blowers. Oil particles/droplets in the diameter distribution were used. The mean diameter is 1.545 μm. The diameter range is from 0.75 μm to 4 μm. Spectral processors (BSA) were used for signal processing, yielding data rates between 500–2000 Hz. Subsequent processing, especially for estimation of the Reynolds stress terms, demanded coincidence of each particle in the two volumes.

3. Computational method

Three-dimensional (3D) RANS computations of the entire section including swirl generation system and annular part of the pipe entering the flue have been performed using commercial CFD-software FLUENT, Grundmann (2003). Separate 3D and 2D, axisymmetric RANS computations of the swirling flow in the concentric annuli part of the inlet system have also been conducted. In addition, the Large-Eddy Simulations of some selected flow cases of the latter configuration ($Re_c = 50{,}500$; $S = 0.0$, 0.6 and 1.1) were performed.

3.1. Mathematical model

The continuity equation and equation of motion governing the weakly compressible flow in the experimentally investigated inlet section of a model swirl combustor take the following integral forms in the inertial coordinate frame:

$$\int_S \rho U_j n_j \, \mathrm{d}S = 0 \tag{2}$$

$$\frac{\partial}{\partial t}\int_V \rho U_i \, \mathrm{d}V + \int_S \rho U_i U_j n_j \, \mathrm{d}S = \int_S T_{ij} n_j \, \mathrm{d}S \tag{3}$$

The stress tensor T_{ij} reads as follows in the LES framework ($T_{ij} \to \overline{T_{ij}}$, $U_i \to \overline{U_i}$):

$$\overline{T_{ij}} = -\overline{P}\delta_{ij} + 2\mu\overline{S}_{ij} - \rho\tau_{ij} \tag{4}$$

The overbar in Eq. (4) denotes the filtered quantities. Hereby, the filter width is determined implicitly by a representative mesh size: $\Delta = (\Delta_x\Delta_y\Delta_z)^{1/3}$. $\overline{S_{ij}} = 0.5(\partial\overline{U_i}/\partial x_j + \partial\overline{U_j}/\partial x_i)$ denotes the rate of strain of the resolved motion. The influence of the unresolved turbulent scales on the resolved ones expressed through the subgrid-scale (SGS) tensor τ_{ij} was modelled by employing the Boussinesq's formulation based on the SGS turbulent viscosity, Smagorinsky (1963):

$$\nu_t = (C_S\Delta)^2|\overline{S_{ij}}| \tag{5}$$

In the present work, the dynamic procedure (Germano et al., 1991) was used for the determination of the Smagorinsky constant C_S.

The stress tensor T_{ij} takes the following time-averaged form in the framework of the RANS approach

$$T_{ij} = -P\delta_{ij} + 2\mu S_{ij} - \rho\overline{u_i u_j} \tag{6}$$

The rate of strain of the time-averaged velocity field U_i is given by $S_{ij} = 0.5(\partial U_i/\partial x_j + \partial U_j/\partial x_i)$. The Reynolds stress tensor $\overline{u_i u_j}$ is defined by a turbulence model. The calculations of an extremely complex flow in the present configuration (recirculating regions, strong streamline curvature originating from geometry shape – longitudinal streamline curvature – and swirl) are very demanding for the turbulence models. A two-layer version of the basic high-Reynolds number second-moment closure (SMC) model due to Gibson and Launder (1978, GL) and its near-wall extension due to Hanjalic and Jakirlic (1998, HJ) have been used in the present work. The former Reynolds stress model implemented in the FLUENT code was modified by introducing the variable model coefficients into the pressure scrambling term in line with the Launder and Shima model (1989). Hereby, the so-called "enhanced wall treatment" was used. This procedure implies employment of a one-equation turbulence model based on the solution of the equation governing the kinetic energy of turbulence due to Wolfstein (1969) in the immediate wall vicinity (near-wall layer). The interface between this and the outer layer employing the modified GL model is positioned in the region where Reynolds number $Re_y = k^{1/2}y/\nu \approx 200$, with k and y being the kinetic energy of turbulence and wall distance, respectively. The near-wall Reynolds stress model of Hanjalic and Jakirlic (1998) contains the modifications for viscosity and wall blockage effects modelled in terms of invariant local turbulence parameters, such as invariants of the anisotropy of Reynolds stress and dissipation-rate tensors, as well as turbulence Reynolds number. In addition to satisfying most of the basic physical constraints, the model was successfully validated in a broad variety of non-equilibrium flows featuring different phenomena: a series of attached, separating and swirling flows in a wide range of Re-numbers and swirl intensities, see e.g., Hanjalic and Jakirlic (1998, 2002). For the sake of brevity no model specification will be given here. Potential readers should consult the original references for more details.

3.2. Numerical method and computational details

Fig. 6 shows the computational grid of the entire inflow system (entrance chamber, swirl generator and annular inlet section) for the maximum swirl number $S \approx 1.2$, for which only tangential channels are present in the swirl

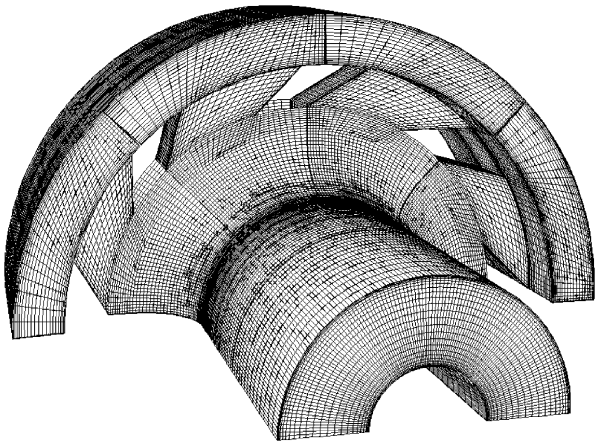

Fig. 6. Numerical grid of the swirl generator system and concentric annuli section. Position of the movable blocks corresponds to $\xi = 30°$ (highest swirl intensity $S \approx 1.2$).

generator ($\xi = 30°$). Hereby, only one eighth of the configuration, meshed by ca. 150,000 cells, was accounted for. These computations were performed by using the commercial code FLUENT. The periodic boundary conditions were applied in the circumferential direction. The geometry includes an annular section of the entrance chamber, allowing the initial condition to be well defined via the prescribed mass flow rate. At the outlet of the co-axial part of the inlet section the pressure boundary conditions were adopted. The so-called "temporal under-relaxation" was applied here to strengthen the diagonal dominance of the coefficient matrix, implying that actually unsteady computations were performed. However, such an unsteady calculation ended up, as expected, in a steady solution.

In addition to the computations of the complete inflow system (Section 4.1), separate computations of the swirling flow in the annular pipe section (geometry of a concentric annulus) were performed (Section 4.3). The latter computations assumed fully developed flow conditions (periodic inlet/outlet boundary conditions were applied), whereby the (equilibrium) swirling motion was created by introducing a fictitious pressure gradient into the momentum equation governing the circumferential velocity. The magnitude of the pressure gradient (with constant value over the cross-section) was iteratively adjusted until the computed U- and W-velocity fields satisfied the prescribed swirl intensity (Eq. 1). Admittedly, the flow conditions in the present annular section deviate strongly from the fully-developed, equilibrium ones. However, since the next step is the Large-Eddy Simulation of the combustor itself, it was necessary to check this method of the inflow data generation (instantaneous velocity field has to be generated for a LES), without performing the extremely demanding simulations of the swirl generation system. This method have successfully been applied for generating the swirling inflow in the LES of Roback and Johnsons model combustor, Pierce and Moin (1998), and in the works of García-Villalba et al. (2004) and Wang et al. (2004). In the present work, this method was applied to both the RANS computations (both a 2D axisymmetric and a 3D geometry were considered using the second-moment closure models described previously in Section 3.1; here only the results of the HJ model are shown) and the Large-Eddy simulations of the flow cases with $Re_c = 50{,}500$.

The computer code used for solving the RANS equations employing the HJ near-wall, second-moment closure model is based on the finite volume method for 2D axisymmetric problems using the SIMPLE algorithm for coupling the velocity and pressure fields. The code works with orthogonal grids and collocated variable arrangement. A central differencing scheme is used for the approximation of diffusive fluxes and a blended upwind-central differencing scheme for the discretization of convective fluxes; the latter is implemented in the deferred correction manner. The value of blending factor was 1.0 corresponding to the CDS scheme. Due to the flow symmetry typical for the pipe geometries ($\partial/\partial\theta = 0$), the computational domain has a rectangular form of the length L (can be chosen arbitrarily because of the periodic inlet/outlet conditions) and the height $H = R_{c,o} - R_{c,i} (R = D/2)$. The 2D grid comprises $N_x x N_r = 4x62$ nodes. To get appropriate resolution in the wall-normal direction the grid was squeezed in the near-wall regions, enabling a dimensionless wall distance of the wall-nearest grid point to be $y^+ \leqslant 0.5$.

An in-house computer code FASTEST based on a finite volume numerical method for solving the three-dimensional filtered Navier–Stokes equations on block-structured, body-fitted meshes was used in the LES framework. Block interfaces are treated in a conservative manner, consistent with the treatment of inner cell-faces. A cell centered (collocated) variable arrangement and cartesian vector and tensor components are used. The well-known SIMPLE algorithm was applied for coupling the velocity and pressure fields. Hereby, a second-order central differencing scheme was applied for the spatial discretization and the second-order Crank–Nicolson method for the time discretization. The solution domain length $L_x = 2.67\pi(R_{c,o} - R_{c,i})$ was meshed by a Cartesian grid with $N_x x N_r x N_\Theta = 64x49x128$ grid cells. No-slip boundary conditions were applied at both walls resolving the wall boundary layer with the wall-closest computational node being positioned at $y^+ \approx 0.5$. The CFL number, representing the time step chosen, was less then unity in the entire flow domain: $CFL_{max} \approx 0.85$. The adopted grid resolution provided the spacing $\Delta_x^+ = 120$, $\Delta_r^+ = 0.5$ (inner and outer wall) to $\Delta_r^+ = 50$ (centre of the annular channel) and $\Delta_\theta^+ = 30$ (inner wall) to $\Delta_\theta^+ = 75$ (outer wall). Admittedly, the grid size (ca. 400000 grid cells) is somewhat coarser then it would be required for the given Reynolds number (one should recall here that the Reynolds number based on the annular channel height $H = R_{c,o} - R_{c,i}$ is $Re_H \approx 25{,}000$). However, as already emphasized, the main purpose of the LES was the validation of the method for the generation of the instantaneous swirling inflow (Section 4.3) based on the reference experiment in relation to the

future simulations of the combustor flow. Therefore, the grid adopted can be regarded as sufficiently fine with respect to the latter issue.

4. Results and discussion

4.1. Preliminary calculations

Before commencing with the measurements a detailed numerical investigation of the swirl generator system with annular pipe section has been performed using commercial CFD-software FLUENT. The computations were conducted for all Reynolds numbers and swirl intensities given in Table 1. The flow configuration obtained at $Re_c = 125{,}500$ (mass flow rate $\dot{m}_c = 0.25\,\mathrm{kg/s}$) and $S = 1.2$ is illustrated representatively by the mean streamlines and mean velocity contours in Figs. 7 and 8, respectively.

The streamlines in the co-axial part of the inlet section have been colored by Mach number, exhibiting a low compressibility (Mach number reaches its maximum value about 0.3) as well as regions with local separation. This is also visible in Fig. 8, where the back-flow regions (dark blue areas) are situated within the radial part of the swirl generator. As indicated in the introductory section, this

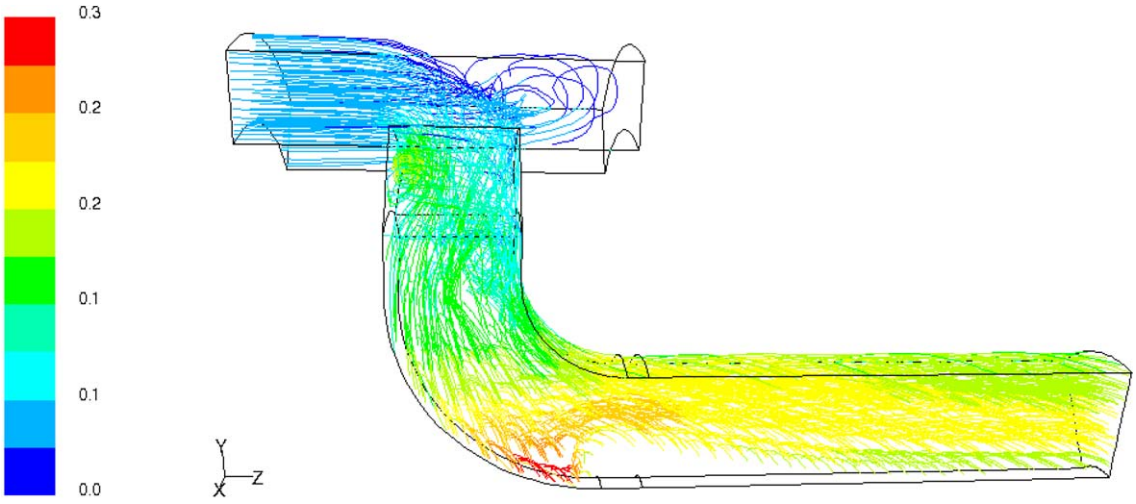

Fig. 7. Streamlines in the co-axial part of the inlet section coloured by Mach number, $Re_c = 125{,}500$, $S = 1.2$.

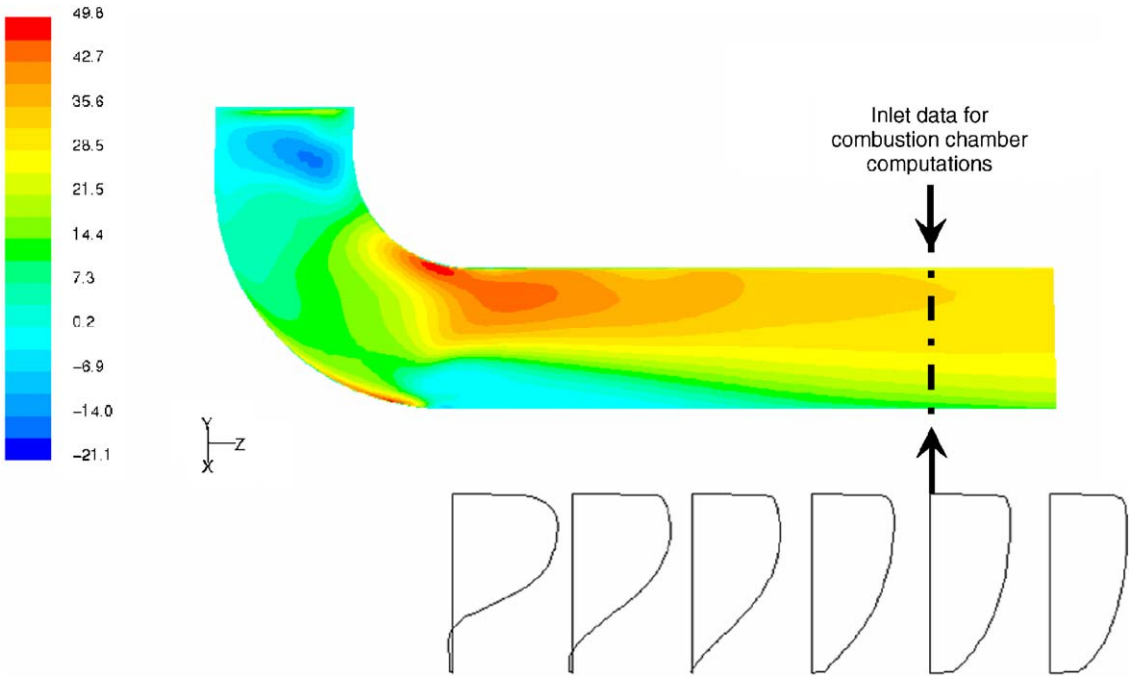

Fig. 8. The axial velocity component (m/s) contours in the co-axial part of the inlet section (upper) and the downstream development of the velocity profile (lower), $Re_c = 125{,}500$, $S = 1.2$.

separation region represents an outcome of the flow past the movable blocks resulting in a vortex shedding of lower frequency due to the effect of confinement. The flow along the outer, convex wall of the 90° turned bend exhibits, as expected, a substantial acceleration due to strong streamline curvature. Contrarily, the flow over the inner, concave wall, exhibiting the so-called destabilizing curvature with respect to the turbulence level, is strongly decelerated. The local separation detected at the inner wall at the very beginning of the straight part of the annular section is induced by the action of a strong swirl. Exactly at this location the transition occurs from the radial motion towards the symmetry axis into the axial motion within the annular section. On the other hand, the swirling motion in the radial part of the swirl generator is strongly accelerated when entering the annular pipe due to the reduction of cross-section. In addition to the adverse pressure gradient effects, evident through flow deceleration, this strong swirl affects the local flow reversal. Fig. 8 shows profiles of the axial velocity component in the co-axial part of the inlet section (left) and the development of the velocity profiles along the length (120 mm) of the extended annular tube (right). The wall-bounded flow reversal is clearly indicated by negative values of the axial velocities. The flow approaches a fully developed state at a length of 80mm for these high swirl conditions. The inlet data have been taken 40 mm upstream of the expansion and compared with the measurements in Section 4.3, Figs. 12 and 13.

4.2. Experimental results

The measured velocity and Reynolds stress profiles (at the cross-section located 40 mm upstream of the expansion) are shown from the inner side (left) to the outer side (right) across the annular inlet in Figs. 9–11. All results are normalised using the bulk axial velocity within the co-axial part of the inlet section U_c. The results shown are taken at a Reynolds number in the annular channel of $Re_c = 125{,}500$ over a range of swirl intensities. Three different sets of results with respect to the three different mass flow rates of the mean flow within the central pipe are displayed.

4.2.1. Mean velocity field

Both the axial and tangential velocities (Fig. 9) are relatively insensitive to the inner jet flow velocity. The axial velocity corresponding to the non-swirling flow exhibits a fairly uniform profile at a value $U/U_c \approx 1$, being characterized by a weak negative gradient in the flow core. Such a slightly asymmetric velocity profile is a consequence of the transverse shear whose magnitude increases with the curvature of the inner cylinder. The wall shear stress at the inner wall becomes larger then the one at the outer wall. This result is in good qualitative agreement with the results of the Direct Numerical Simulation of the non-swirling flow in a concentric annulus performed by Chung et al. (2002). With increasing swirl number the formation of the swirl can be understood quite easily and provide information about the development of the axial velocity and the sign of the gradient of the inner flow.

The major result from the present measurements, as far as the swirling configuration is concerned, is that the axial velocity increases from the inside to the outside wall as a consequence of the increased swirl intensity. This is also manifested through the boundary-layer thickening along the lower wall. Such behaviour is in contrast to the non-swirling case. Furthermore, the maximum of the velocity profile moves towards the outer wall. This is especially true for the highest swirl intensity, where a local separation at the inner wall of the 90°-turned bend occurs. The velocity gradient in the flow core becomes positive and increases substantially as a function of increased swirl intensity. This gradient is almost constant in the lower half of the cross-section, being in line with the linear behaviour of the mean axial velocity. It is important to note that the region with the positive gradient of the axial velocity spreads towards the outer wall, contributing decisively to the increased turbulence level (see e.g., Fig. 10). In contrast to this, the wall

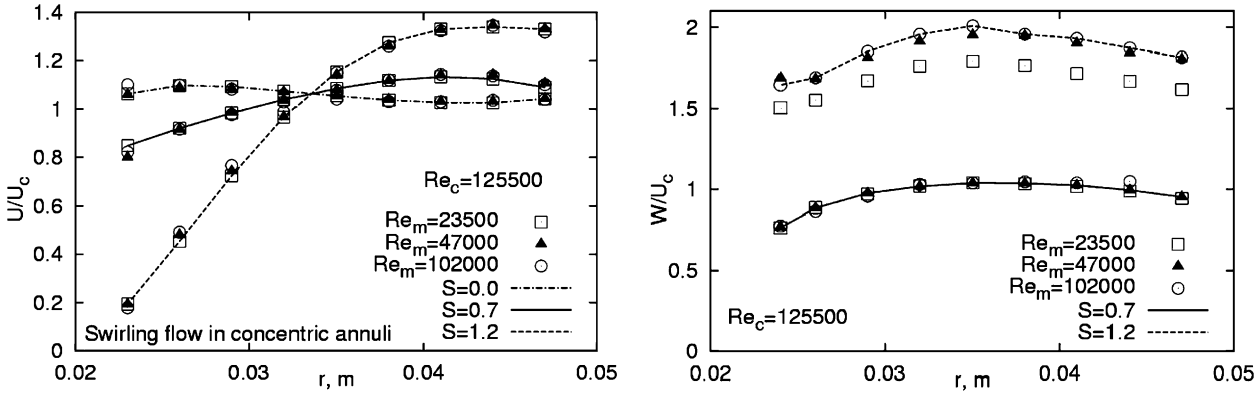

Fig. 9. Normalised axial (U/U_c) and tangential (W/U_c) velocities in the annular flow for a Reynolds number of the coaxial flow $Re_c = 125{,}500$ in a range of swirl intensities $S = 0.0$–1.2 in relation to the Reynolds number of the main flow.

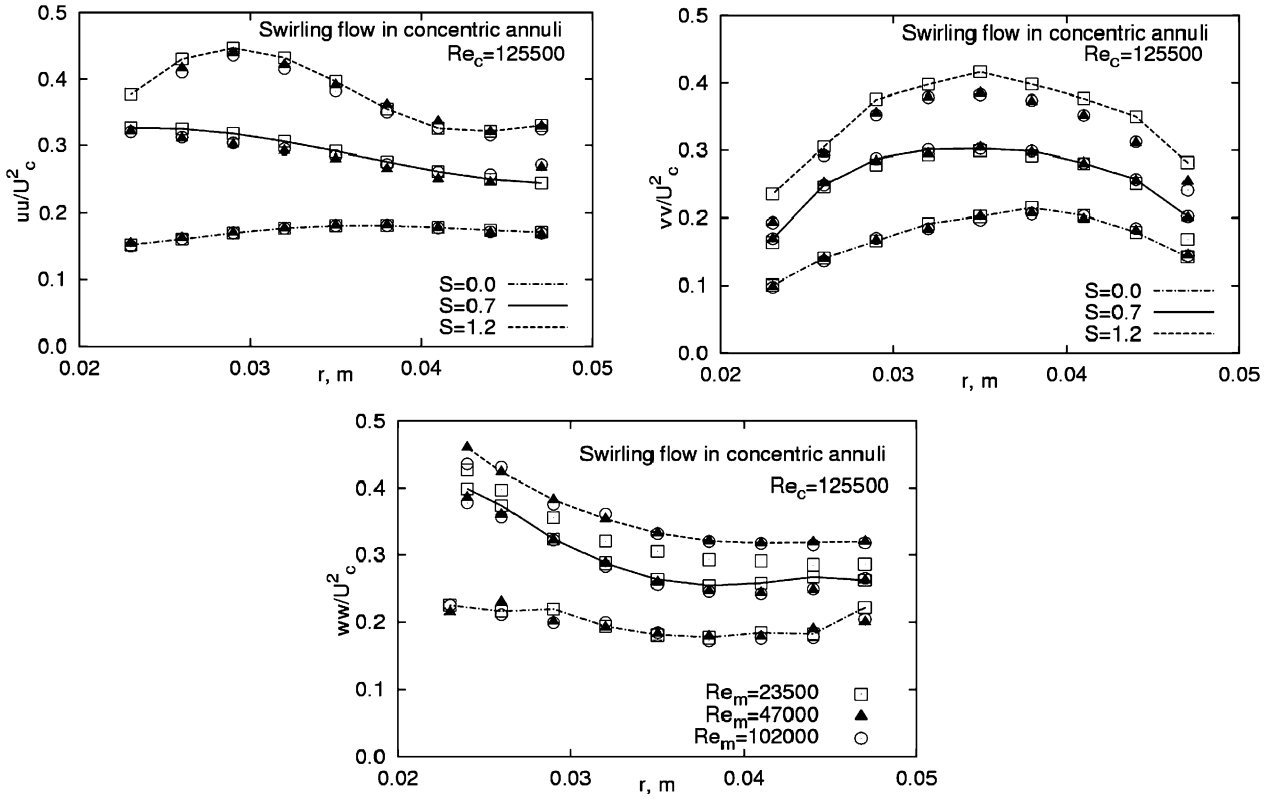

Fig. 10. Normal Reynolds stress components $\overline{uu}/U_c^2$, $\overline{vv}/U_c^2$ and $\overline{ww}/U_c^2$ in the annular flow for a Reynolds number of the coaxial flow $Re_c = 125{,}500$ in a range of swirl intensities $S = 0.0$–1.2 in relation to the Reynolds number of the main flow.

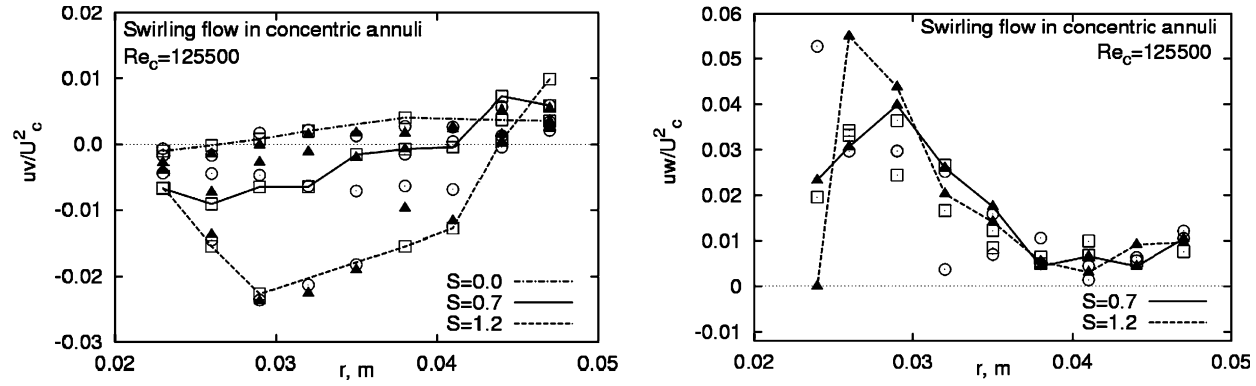

Fig. 11. Shear stress components $\overline{uv}/U_c^2$ and $\overline{uw}/U_c^2$ in the annular flow for a Reynolds number of the coaxial flow $Re_c = 125{,}500$ in a range of swirl intensities $S = 0.0$–1.2 in relation to the Reynolds number of the main flow.

gradient of the axial velocity and consequently the wall shear stress decrease from the inside to the outside of the annular flow. Reynolds number effects on the mean flow field could be to a certain extent deduced by comparing the results presented in Fig. 9 ($Re_c = 125{,}500$) and Fig. 12 ($Re_c = 50{,}500$). Apart from the lower velocity magnitude, which leads to a lower wall shear stress at the inner wall (the corresponding velocity profile for the highest swirl intensity also indicates possible flow separation) and a somewhat reduced turbulence level (compare Figs. 10 and 13), these effects are not too pronounced. The tangential velocity profiles indicate the so-called free-vortex type of the swirling motion, Fig. 9 (lower). The maximum tangential velocity is formed approximately in the middle of the annular channel. Similar as in the case of the axial velocity, the tangential velocity profiles indicate a lower wall shear stress (determined by the tangential velocity gradient) at the inner wall and a higher wall shear stress at the outer wall. Such behaviour reflects the stable (inner wall) and unstable (outer wall) curvature effects.

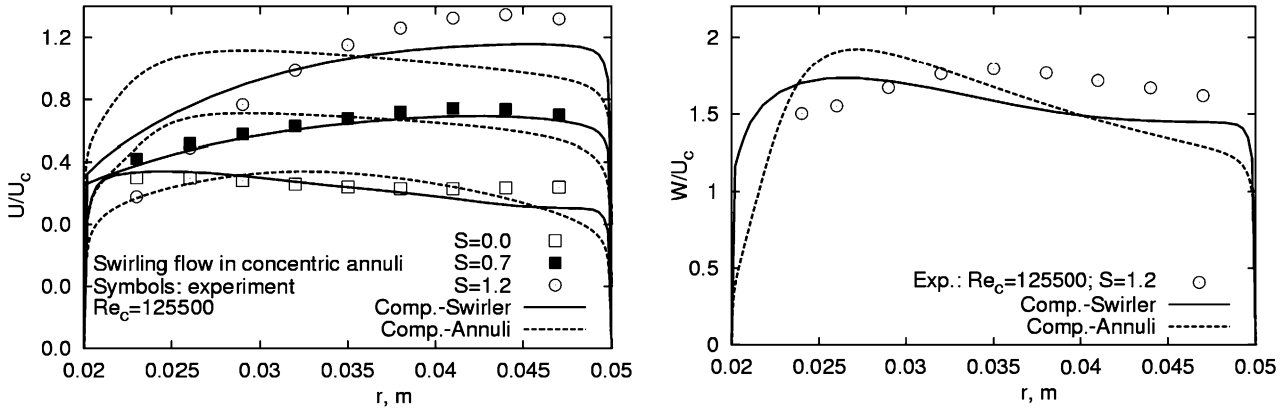

Fig. 12. Axial velocity profiles for range of the swirl numbers (left) and circumferential velocity profiles for the case with strongest swirl (right): comparison between experiments and RANS computations.

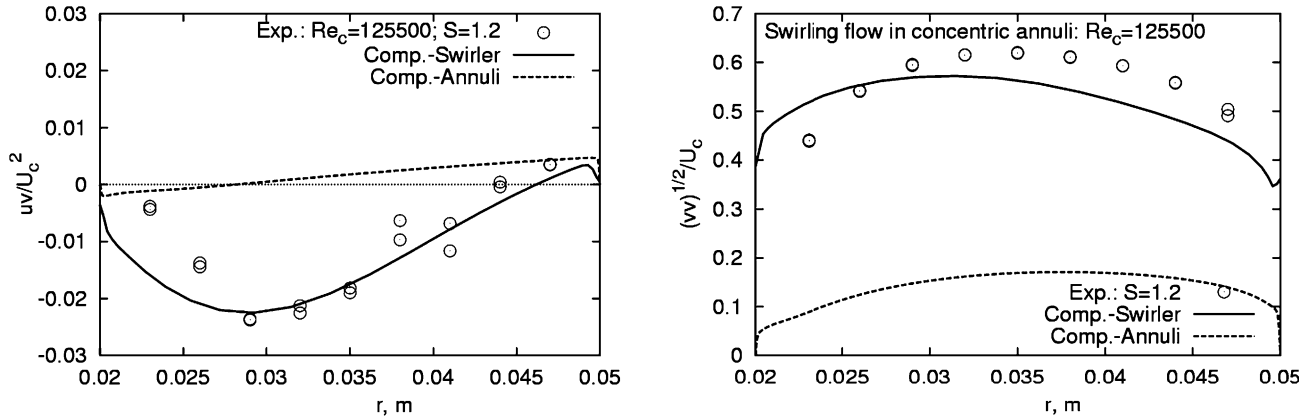

Fig. 13. Shear stress $\overline{uv}/U_c^2$ (left) and normal-to-the-wall turbulence intensity $\sqrt{\overline{v^2}}/U_c$ (right) in the concentric annulus of the inlet section of the present model combustor: comparison between experiments and RANS computations.

4.2.2. Reynolds stress field

All of the Reynolds stresses $\overline{uu}$, $\overline{vv}$, $\overline{ww}$, $\overline{uv}$, $\overline{vw}$ (not measured) and $\overline{uw}$ are non-zero. Selected results of the Reynolds stress measurements are shown in Figs. 10 and 11. Profiles of all three normal stress components (Fig. 10) indicate a clear tendency towards intensification of the turbulence production with increased swirl intensity. As pointed out in the introduction, the turbulence level in the annular channel is additionally influenced by the complex strain rates of the flow in the swirl generation system. Even the non-swirling case exhibits a much higher turbulence level then the one typically encountered in a generic annular flow, e.g., Clayton and Morsi (1985) and Yowakim and Kind (1988). It should be further noted, that the increased stress level is partially due to effects of the sudden flow expansion (adverse pressure gradient effects), occurring only 40 mm downstream of the measurement station. Apart of these influences, contributing mostly to the high turbulence level in the flow core (note the absence of the clear profile minima in this flow region), the behaviour of the normal stress components follows closely the changes in mean velocity gradients. It should be recalled here, that the structure of a swirling flow is strongly influenced by the secondary shearing ($\partial W/\partial r$) and streamline curvature ($-W/r$) in addition to the mean shear ($\partial U/\partial r$). The profile shapes could be appropriately analyzed by looking at the stress production rates (in this consideration, the streamwise changes are neglected, as well as the radial motion): $P_{11} \approx -2\overline{uv}\partial U/\partial r$, $P_{22} \approx 2\overline{vw}W/r$ and $P_{33} \approx -2\overline{vw}\partial W/\partial r$. Despite the fact that both velocity gradients experience a certain reduction at the inner wall leading to a consequent weakening of the turbulence intensity in the immediate wall vicinity (this effect was not captured by experiment), the turbulence level increases in the outer inner-wall region due to boundary layer thickening (see e.g., Fig. 9), as in the boundary layers affected by an adverse pressure gradient. The position of the peak value of the streamwise stress component (Fig. 10 upper) is shifted from the wall towards the middle of the annular channel.

It is also obvious when looking at the turbulent stress levels for both swirling configurations, that an increased swirl promotes an isotropic state of turbulence. Similar

for the mean flow, the increased flow rate of the central jet has not significantly influenced the results. A slight deviation is noted only for the case with the strongest swirl. Despite a certain scatter of the experimental results of the two shear stresses $\overline{uv}$ and $\overline{uw}$, their global behaviour can be clearly recognized. The portion of the cross-section with a negative production of the shear stress $\overline{uv}$, corresponding to the positive gradient of the axial velocity ($P_{12} \approx -\overline{v^2}\partial U/\partial r + \overline{uw}W/r$), thickens with the increased swirl. Hereby, the position of the zero shear stress value moves towards the outer wall, following closely the behaviour of the maximum ($\partial U/\partial r = 0$) of the axial velocity profile, Fig. 9 (left). The strongest production of the shear stress $\overline{uw}$ ($P_{13} \approx -\overline{uv}\partial W/\partial r - \overline{vw}\partial U/\partial r$) occurs in the region of the inner wall characterized by strong (positive) gradients of both axial and circumferential velocity (note a negative value of the shear stress $\overline{vw}$ deduced from the computational work, Fig. 14, right).

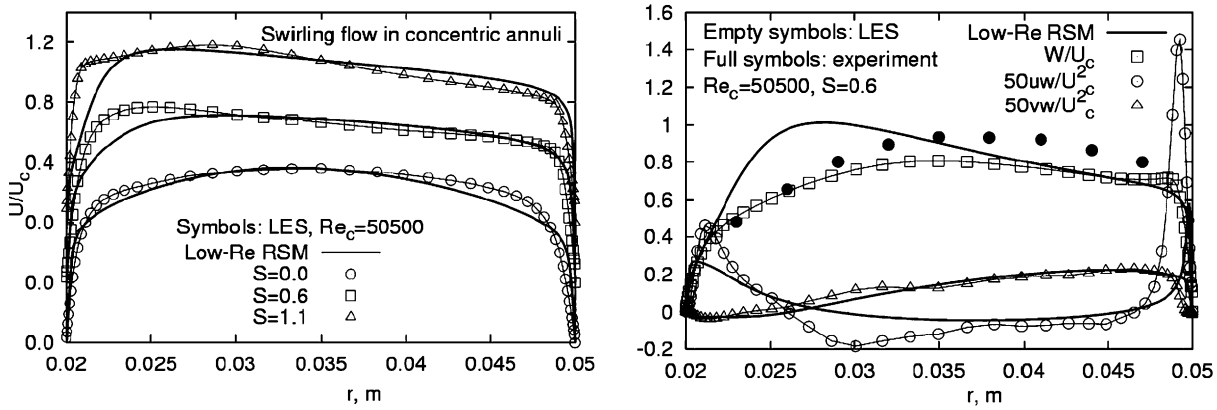

Fig. 14. Axial velocity U/U_c (left), circumferential velocity W/U_c and shear stress profiles $\overline{uw}/U_c^2$ and $\overline{vw}/U_c^2$ (right) in the concentric annulus of the inlet section of the present model combustor: comparison between experiments, LES and RANS computations.

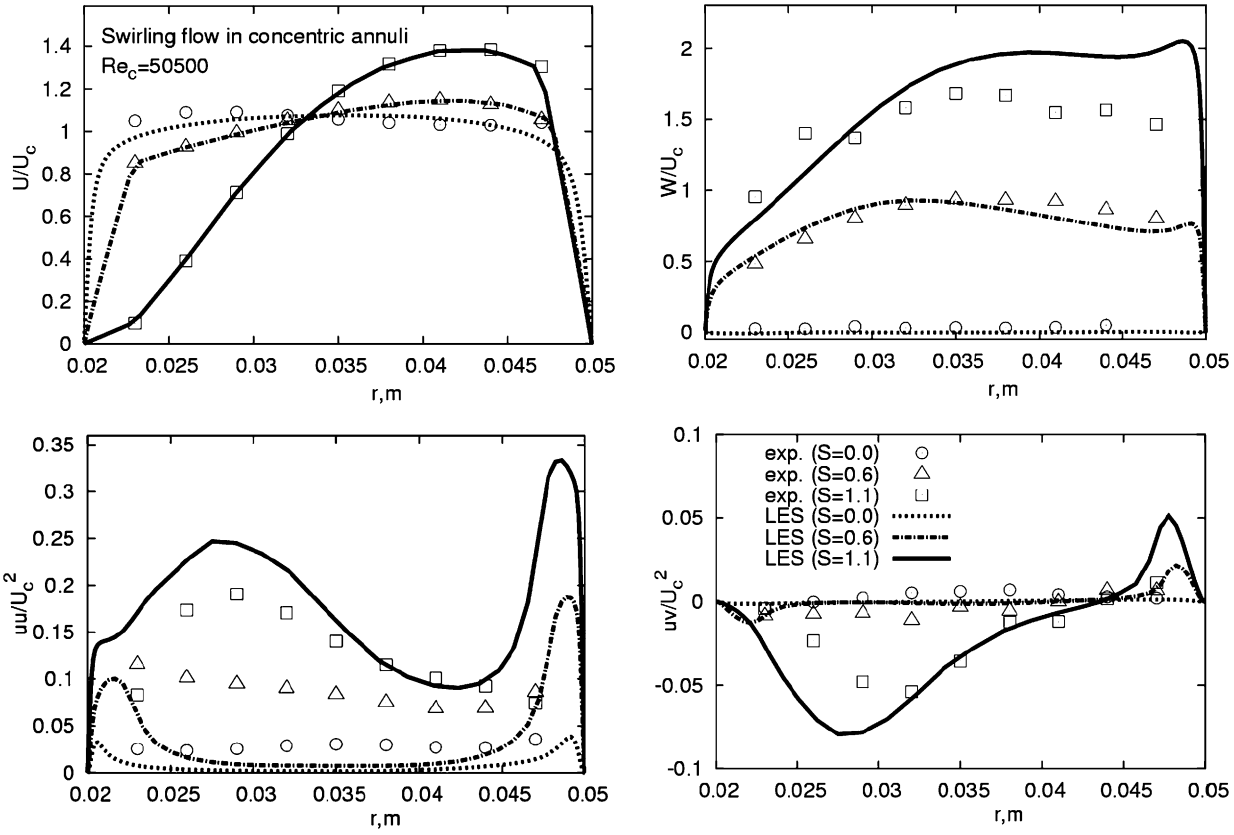

Fig. 15. Axial (U/U_c) and circumferential (W/U_c) velocity, streamwise ($\overline{uu}/U_c^2$) and shear ($\overline{uv}/U_c^2$) stress profiles in the concentric annulus of the inlet section of the present model combustor obtained by LES with forcing in the axial direction.

4.3. Comparison of experimental and numerical results

Whereas the swirling part of the flow (circumferential velocity and two associate shear stresses, Figs. 12[3] and 14 right) obtained by computing (using both RANS and LES) the flow in the concentric annulus assuming the fully-developed conditions agrees reasonably with experimental results, the axial velocity component retains a profile form corresponding to the non-swirling flow in a concentric annulus, exhibiting the opposite (negative) gradient over a large portion of the cross-section, see Fig. 12 (left) and 14 (left). Accordingly, the turbulent stresses agree poorly with the reference data (Fig. 13). The effect of the wrong gradient of the axial velocity is mostly visible on the $\overline{uv}$-profile (Fig. 13 (left)) displaying a zero value at the point of the maximum axial velocity, which is in large disagreement with the experimental results. The possible reason is the weak influence of the circumferential velocity on the axial velocity, whose transport equations include no common variables for the fully-developed flow conditions. The only (indirect) connection between U- and W-equations occurs through the equations for the shear stress components $\overline{uv}$ and $\overline{vw}$. As noted earlier, it is obvious (see also Figs. 7 and 8) that the experimental flow conditions depart significantly from the fully developed conditions assumed. Pierce (2001) introduced a further correction being equivalent to adding an appropriately defined body force into the U-component momentum equation in order to obtain the proper U-velocity profile. This practice assumes the mean statistical properties having been specified, e.g., from experiment. This additional forcing was also applied in the present work. At each time step, the streamwise-averaged velocity component $\overline{U}(y,z,t) = \langle U(x,y,z,t)\rangle_x$ was computed. Than, the instantaneous streamwise velocity field was constrained in a way, that it has the specified mean velocity profile $U(y,z)$:

$$U(x,y,z,t) \rightarrow U(x,y,z,t) - \overline{U}(y,z,t) + U(y,z)$$

Fig. 15 displays the axial and circumferential velocities and the Reynolds stresses $\overline{u^2}$ and $\overline{uv}$ obtained by doing so. The behaviour of both stresses, especially the shear stresses is now much closer to the experimentally obtained results (e.g., compare this result with $\overline{uv}$ stress presented in Fig. 13(left)). Nevertheless, some further investigations are necessary. It would be, e.g., possible to introduce similar forcing onto the streamwise stress component. As expected, the SMC results obtained by accounting for the swirl generator system reproduced all important mean flow and turbulent features in reasonable agreement with available experimental data (solid lines in Figs. 12 and 13).

[3] The abbreviation "Comp.-Swirler" denotes the computational results obtained for the complete swirl generator system obtained by using a two-layer version of the GL model (Section 4.1). The denotation "Comp.-Annuli" is related to the computations of the "fully-developed" swirling flow in the annular pipe by using the HJ model.

5. Conclusions

The flow structure in the annular section of the inlet system of a swirl combustor with respect to the Reynolds number and swirl intensity influence was investigated experimentally and numerically. The velocity field in the inlet section was measured using the laser Doppler measurement technique. The RANS–SMC results obtained by computing the complete inflow system accounting for the swirl generator agree reasonable well with the experimental results for both mean flow and turbulence quantities. The separate RANS–SMC and LES computations of the swirling annular pipe flow imposing the fully developed flow conditions in line with the method for generating the swirling inflow proposed by Pierce and Moin (1998) were also performed. Whereas the (concentrated-vortex type) circumferential velocity field and associated shear stress components were in good agreement with the experimental results as well as in good mutual agreement, the axial velocity profile, obtained by both the RANS–SMC and LES methods, exhibits the wrong shape indicating the negative velocity gradient, typical for the non-swirling flow in a concentric annulus. It was shown that an additional forcing introduced into the momentum equation in the streamwise direction could improve this behaviour. Nevertheless, further investigations related to appropriate corrections are necessary.

Acknowledgements

The financial support of the German Ministry for Education and Science (BMBF) through the grant 03TRA2AC (R. Palm) and the German Scientific Foundation (DFG) through the grant JA 941/7-1 (S. Šarić) is gratefully acknowledged.

References

Chung, S.Y., Rhee, G.H., Sung, H.J., 2002. Direct numerical simulation of turbulent concentric annular pipe flow. Part 1: Flow field. Int. J. Heat Fluid Flow 23, 426–440.

Chung, S.Y., Sung, H.J., 2005. Large-eddy simulation of turbulent flow in a concentric annulus with rotation of an inner cylinder. Int. J. Heat Fluid Flow 26, 191–203.

Clayton, B.R., Morsi, Y.S.M., 1984. Determination of principal characteristics of turbulent swirling flow along annuli. Part 1: Measurement of time mean parameters. Int. J. Heat Fluid Flow 5 (4), 195–203.

Clayton, B.R., Morsi, Y.S.M., 1985. Determination of principal characteristics of turbulent swirling flow along annuli. Part 2: Measurement of turbulence components. Int. J. Heat Fluid Flow 6 (1), 31–41.

Dellenback, P.A., Metzger, D.E., Neitzel, G.P., 1988. Measurements in turbulent swirling flow through an abrupt axisymmetric expansion. AIAA J. 26 (6), 669–681.

FLUENT Version 6.0, User Manual, 2001.

García-Villalba, M., Fröhlich, J., Rodi, W., 2004. On inflow boundary conditions for large eddy simulation of turbulent swirling jets. In: 21st International Congress of Applied and Theoretical Mechanics, Warsaw, Poland.

Germano, M., Piomelli, U., Moin, P., Cabot, W.H., 1991. A dynamic subgrid-scale eddy-viscosity model. Phys. Fluids 3 (7), 1760–1765.

Gibson, M.M., Launder, B.E., 1978. Ground effects on pressure fluctuations in the atmospheric boundary layer. J. Fluid Mech. 86, 491–511.

Grundmann, S., 2003. Numerische Untersuchung drallbehafteter Strömungen in einem realitätsnahen Drallbrennermodell. Diploma thesis, Darmstadt University of Technology (presented at the DGLR Kongress, 2004).

Hanjalic, K., Jakirlic, S., 1998. Contribution towards the second-moment closure modelling of separating turbulent flows. Comput. Fluids 27, 137–156.

Hanjalic, K., Jakirlic, S., 2002. Second-Moment Turbulence Closure Modelling. In: Launder, B.E., Sandham, N.H. (Eds.), Closure Strategies for Turbulent and Transitional Flows. Cambridge University Press, Cambridge, UK, pp. 47–101.

Hassa, C., Migueis, C.E., Voigt, P., 1998. Design Principals for the Quench Zone of Rich-Quench-Lean Combustors. AGARD PEP-Symp. on Design Principles and Methods for Aircraft Gas Turbine Engines, Toulouse, France, May 11–15.

Heitor, M.V., Whitelaw, J.H., 1986. Velocity, temperature, and species characteristics of the flow in a gas-turbine combustor. Combust. Flames 64, 1–32.

Hogg, S., Leschziner, M.A., 1989. Computation of highly swirling confined flow with a Reynolds stress turbulence model. AIAA J. 27 (1), 57–63.

Jakirlic, S., Jester-Zürker,R., Tropea, C., 2002. Report on 9th ERCOFTAC/IAHR/COST Workshop on Refined Turbulence Modelling. October, 9–10, 2001, Darmstadt University of Technology, ERCOFTAC Bulletin, 55, 36–43.

Lai, Y.G., 1996. Predictive capabilities of turbulence models for a confined swirling flow. AIAA J. 34 (8), 1743–1745.

Leuckel, W., 1969. Swirl intensities, swirl types and energy losses of different swirl generating devices. IFRF Doc. Nr. G02/a/16.

Launder, B.E., Shima, N., 1989. Second-moment closure for the near-wall sublayer: Development and application. AIAA J. 27 (10), 1319–1325.

Nejad, A.S., Vanka, S.P., Favaloro, S.C., Samimy, M., Langenfeld, C., 1989. Application of Laser Velocimetry for Characterization of Confined Swirling Flow. ASME J. Eng. Gas Turbines Power 111, 36–45.

Nouri, J.M., Whitelaw, J.H., 1994. Flow of Newtonian and non-Newtonian fluids in a concentric annulus with rotation of the inner cylinder. ASME J. Fluids Eng. 116, 821–827.

Pierce, C.D., Moin, P., 1998. Method for Generating Equilibrium Swirling Inflow Conditions. AIAA J. 36 (7), 1325–1327.

Pierce, C.D., 2001. Progress-variable approach for Large-Eddy Simulation of turbulent combustion. Ph.D., Thesis, Stanford University.

Roback, R., Johnson, B.V., 1983. Mass and Momentum Turbulent Transport Experiments with Confined Swirling Coaxial Jets. NASA Contractor Report 168252.

Smagorinsky, J., 1963. General circulation experiments with the primitive equations. Mon. Weather Rev. 91, 99–164.

So, R.M.C., Ahmed, S.A., Mongia, H.C., 1984. An experimental investigation of gas jets in confined swirling air flow. NASA Contractor Report 3832.

Wang, P., Bai, X.S., Wessman, M., Klingmann, J., 2004. Large eddy simulation and experimental studies of a confined turbulent swirling flow. Phys. Fluids 16 (9), 3306–3324.

Wennerberg, D., Obi, S., 1993. Prediction of Strongly Swirling Flows in Quarl Expansions with a Non-Orthogonal Finite-Volume Method and a Second-Moment Turbulence Closure. Eng. Turbulence Modelling Exper. 2, 197–206.

Wolfstein, M., 1969. The velocity and temperature distribution in one-dimensional flow with turbulence augmentation and pressure gradient. Int. J. Heat Mass Trans. 12, 301–318.

Yowakim, F.M., Kind, R.J., 1988. Mean flow and turbulence measurements of annular swirling flows. ASME J. Fluids Eng. 110, 257–263.